Front. Optoelectron. 2012, 5(4): 414–428
DOI 10.1007/s12200-012-0280-z

RESEARCH ARTICLE

Competition mechanism of multiple four-wave mixing in highly nonlinear fiber: spatial instability and satellite characteristics

Liang ZHAO (✉)[1], Junqiang SUN[2], Xinliang ZHANG[2], Cong CHEN[3]

1 Wuhan Foreign Languages School, Wuhan 430022, China
2 Wuhan National Laboratory for Optoelectronics, School of Optoelectronic Science and Engineering, Huazhong University of Science and Technology, Wuhan 430074, China
3 Naval University of Engineering, Wuhan 430033, China

Abstract Competition mechanism in multiple four-wave mixing (MFWM) processes is demonstrated theoretically. Provided considering only two waves injected into a highly nonlinear fiber (HNLF), there are three modes displaying comprehensive dynamic behaviors, such as fixed points, periodic motion, and chaotic motion. Especially, Mode C of MFWM is emphasized by analyzing its phase-space trajectory to demonstrate nonlinear wave-wave interactions. The study shows that, when the phase-space trajectory approaches or gets through a saddle point, a dramatic power depletion for the injected wave can be realized, with the representative point moving chaotically, but when phase-space trajectories are distributed around a center point, the power for the injected wave is retained almost invariable, with the representative point moving periodically. Finally, the evolvement of satellite wave over an optical fiber is investigated by comparing it with the interference pattern in Young's double-slit experiment.

Keywords highly nonlinear fiber (HNLF), periodic motion, representative point, Young's double-slit experiment

1 Introduction

Four-wave mixing (FWM), the most pervasive and persuasive modern technology in optical communication, marked by rapid change and growth, is moving into a new era, an era of extraordinary sophistication and versatility. It enjoys the obvious advantage of generating new frequencies, giving rise to a potential breakthrough in the applicative regime, such as broadcast all-optical wavelength conversion [1,2], fiber optical parametric amplification (FOPA) [3,4], all-optical switching [5,6], and 2R regeneration [7,8].

With the rapid development of multiple four-wave mixing (MFWM) theory, it has attracted increasing attention from experimentalists and theorists alike. Liu et al. have developed MFWM in theory and experiment when pump waves have equal frequency spacing, and have found the self-stability effect in optical fibers under the undepleted approximation [9,10]. Moreover, Cappellini and Trillo have investigated the degenerate FWM effect in a strong-interaction regime [11], with the aid of Hamilton system and phase-space trajectory. Similar investigations can be found in Refs. [12–14]. In fact, when taking account of two waves injected into a piece of highly nonlinear fiber (HNLF) and the occurrence of the high conversion efficiency, there are three sub-FWM processes, corresponding to three modes, existing in HNLF, as seen in Fig. 1. Moreover, the above three modes will interact and compete with each other, leading to energy switching from one wave to another in the largest extent.

An important phenomenon in MFWM is the power-depletion effect, which can find many applications in optical communications system, such as all-optical switching and notch filter. In Ref. [15], we theoretically demonstrated a novel notch filter using the dramatic power-depletion effect in HNLF, which can filter out the undesired wave through switching its energy to other waves. In experiment, Marhic et al. realized 92% pump depletion in a continuous-wave FOPA [16], with a 200 mW pump at 1560 nm in an 11 km dispersion-shifted fiber. In our paper, we put forward the competition-mechanism conception in MFWM processes, and we

Received July 20, 2012; accepted August 30, 2012

E-mail: liangshao_acool@smail.hust.edu.cn

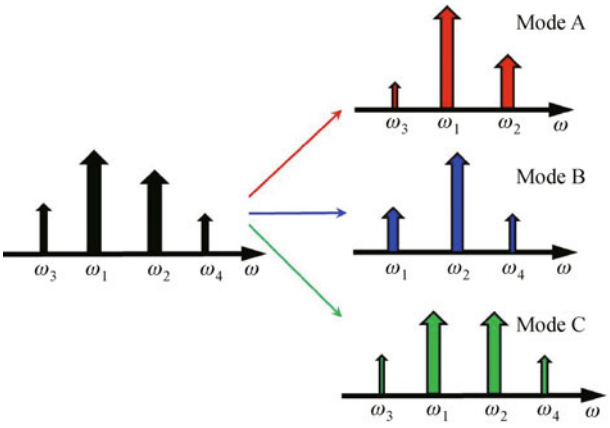

Fig. 1 Schematic diagram for the decomposition of MFWM

investigate Mode C of MFWM in detail by yielding the phase-space equation and the fixed points analytically from the coupled-wave equations to analyze the stability of the system. Furthermore, we discuss the stability of the conserved system (referred to the MFWM system) by deriving the equilibrium points from the potential well equation analytically. At last, the evolvement of satellite wave over an optical fiber is compared with Young's double-slit experiment [17,18], and the analytical expressions, describing periodic and amplitude characteristics of satellite wave, are yielded, which can explain the physical implication of the dynamical process.

2 Competition mechanisms in MFWM processes

Figure 1 illustrates three modes in HNLF, which indicates that MFWM processes can be decomposed into three sub-FWM processes, namely Mode A, Mode B and Mode C, whose angular frequency relations satisfy $2\omega_1 = \omega_2 + \omega_3$, $2\omega_2 = \omega_1 + \omega_4$, $\omega_1 + \omega_2 = \omega_3 + \omega_4$, respectively. One can easily obtain the following conclusion based on Ref. [9]: when the center wavelength in terms of the injected wavelength is just located at around the zero-dispersion wavelength, Mode A will play a dominate role in MFWM processes when $P_1 >> P_2$, and Mode B will occupy the absolute advantage when $P_2 >> P_1$. Last but not least, Mode A and Mode B will be in dynamical balance when $P_1 = P_2$ ($P_1 \approx P_2$), and then Mode C will dominate in the whole process. When neglecting the walk-off, absorption, and dispersion effects in HNLF, the coupled-wave equations can be robustly expressed as

$$\begin{aligned}\frac{dA_1}{dz} &= i\gamma[|A_1|^2 + 2(|A_2|^2 + |A_3|^2 + |A_4|^2)]A_1 \\ &\quad + 2i\gamma A_1^* A_2 A_3 \exp(i\Delta\beta_1 z) \\ &\quad + i\gamma A_4^* A_2^2 \exp(-i\Delta\beta_2 z) \\ &\quad + 2i\gamma A_2^* A_3 A_4 \exp(i\Delta\beta_3 z), \end{aligned} \tag{1}$$

$$\begin{aligned}\frac{dA_2}{dz} &= i\gamma[|A_2|^2 + 2(|A_1|^2 + |A_3|^2 + |A_4|^2)]A_2 \\ &\quad + 2i\gamma A_2^* A_1 A_4 \exp(i\Delta\beta_2 z) \\ &\quad + i\gamma A_3^* A_1^2 \exp(-i\Delta\beta_1 z) \\ &\quad + 2i\gamma A_1^* A_3 A_4 \exp(i\Delta\beta_3 z), \end{aligned} \tag{2}$$

$$\begin{aligned}\frac{dA_3}{dz} &= i\gamma[|A_3|^2 + 2(|A_1|^2 + |A_2|^2 + |A_4|^2)]A_3 \\ &\quad + 2i\gamma A_4^* A_1 A_2 \exp(-i\Delta\beta_3 z) \\ &\quad + i\gamma A_2^* A_1^2 \exp(-i\Delta\beta_1 z), \end{aligned} \tag{3}$$

$$\begin{aligned}\frac{dA_4}{dz} &= i\gamma[|A_4|^2 + 2(|A_1|^2 + |A_2|^2 + |A_3|^2)]A_4 \\ &\quad + 2i\gamma A_3^* A_1 A_2 \exp(-i\Delta\beta_3 z) \\ &\quad + i\gamma A_1^* A_2^2 \exp(-i\Delta\beta_2 z). \end{aligned} \tag{4}$$

Here, A_j ($j = 1, 2, 3, 4$) is the complex amplitude for each wave, and $\Delta\beta_j$ is the linear phase mismatch profile, which can be analytically derived by expanding the propagation constant in Taylor series [19]. Qualitative and semiquantitative method here is adopted to analyze the energy switching among the waves. Under the circumstances of slowly-varied amplitude approximation and undepleted approximation, we can integrate the first FWM term of Eq. (1) with the result of

$$\begin{aligned} P_1^{1-\mathrm{FWM}} &\approx \left| \int_0^L 2i\gamma A_1^* A_2 A_3 \exp(i\Delta\beta_1 z) dz \right|^2 \\ &\approx \left| 2i\gamma A_1^* A_2 A_3 \int_0^L \exp(i\Delta\beta_1 z) dz \right|^2 \\ &= 16\gamma^2 L^2 P_1 P_2 P_3 \mathrm{sinc}^2\left(\frac{\Delta\beta_1 L}{2}\right), \end{aligned} \tag{5}$$

where $P_1^{1-\mathrm{FWM}}$ represents the amount of power-varying for wave 1 induced by the first FWM term in Eq. (1), and the subscript "1" represents wave 1 while the superscript "1-FWM" denotes the first FWM term, P_j (j = 1, 2, 3, 4) denotes the power of each wave. Similarly, one can yield all the involved FWM terms for $P_i^{j-\mathrm{FWM}}$ ($i = 1, 2, 3, 4$ and j = 1, 2, 3), which are listed in Table 1. Notably, in all the FWM terms, there is a common factor, namely sinc function, featuring oscillation and damping characteristics, which conforms to the experimental results demonstrated

Table 1 Contribution of all the FWM terms to the injected and sideband waves

	1-FWM	2-FWM	3-FWM
1	$16\gamma^2L^2P_1P_2P_3\mathrm{sinc}^2(\Delta\beta_1L/2)$	$4\gamma^2L^2P_4P_2^2\mathrm{sinc}^2(\Delta\beta_2L/2)$	$16\gamma^2L^2P_2P_3P_4\mathrm{sinc}^2(\Delta\beta_3L/2)$
2	$4\gamma^2L^2P_1^2P_3\mathrm{sinc}^2(\Delta\beta_1L/2)$	$16\gamma^2L^2P_2P_4P_1\mathrm{sinc}^2(\Delta\beta_2L/2)$	$16\gamma^2L^2P_1P_3P_4\mathrm{sinc}^2(\Delta\beta_3L/2)$
3	$4\gamma^2L^2P_1^2P_2\mathrm{sinc}^2(\Delta\beta_1L/2)$		$16\gamma^2L^2P_1P_2P_4\mathrm{sinc}^2(\Delta\beta_3L/2)$
4		$4\gamma^2L^2P_2^2P_1\mathrm{sinc}^2(\Delta\beta_2L/2)$	$16\gamma^2L^2P_1P_2P_3\mathrm{sinc}^2(\Delta\beta_3L/2)$

by Hart et al. [20].

Remarkably, Mode A and Mode B have been extensively investigated in the previous literatures [3,10,13] for the degenerate FWM case, but Mode C, corresponding to the non-degenerate FWM, is seldom mentioned before. Differing from the non-degenerate FWM process in a FOPA model, in which three different waves are prerequisite to excite the system, only two different waves are needed for Mode C in our system. Under the conditions of $P_1 \approx P_2$ and $\Delta\beta_1 >> 0$, $\Delta\beta_2 >> 0$, $\Delta\beta_3 \to 0$ [9], Eqs. (1)–(4) are modified to

$$\frac{\mathrm{d}A_1}{\mathrm{d}z} = \mathrm{i}\gamma[|A_1|^2 + 2(|A_2|^2 + |A_3|^2 + |A_4|^2)]A_1 + 2\mathrm{i}\gamma A_2^* A_3 A_4 \exp(\mathrm{i}\Delta\beta_3 z), \tag{6}$$

$$\frac{\mathrm{d}A_2}{\mathrm{d}z} = \mathrm{i}\gamma[|A_2|^2 + 2(|A_1|^2 + |A_3|^2 + |A_4|^2)]A_2 + 2\mathrm{i}\gamma A_1^* A_3 A_4 \exp(\mathrm{i}\Delta\beta_3 z), \tag{7}$$

$$\frac{\mathrm{d}A_3}{\mathrm{d}z} = \mathrm{i}\gamma[|A_3|^2 + 2(|A_1|^2 + |A_2|^2 + |A_4|^2)]A_3 + 2\mathrm{i}\gamma A_4^* A_1 A_2 \exp(-\mathrm{i}\Delta\beta_3 z), \tag{8}$$

$$\frac{\mathrm{d}A_4}{\mathrm{d}z} = \mathrm{i}\gamma[|A_4|^2 + 2(|A_1|^2 + |A_2|^2 + |A_3|^2)]A_4 + 2\mathrm{i}\gamma A_3^* A_1 A_2 \exp(-\mathrm{i}\Delta\beta_3 z). \tag{9}$$

3 Spatial instability

This section focuses on the characteristics of the solutions for Eqs. (6)–(9), and a deeper insight into the spatial instability for nonlinear eigenmodes of interaction is investigated extensively. In fact, as a consequence of the existence of spatially unstable eigensolutions, small variations in certain input conditions lead to quite different spatial evolutions and therefore to dramatically different output power redistributions among the waves. By inserting $A_j = \xi_j \exp(\mathrm{i}\phi_j)$, ($j$ = 1, 2, 3, 4), $\Gamma = \gamma \cdot z$, $\eta = \xi_4^2$ and $\kappa_3 = \Delta\beta_3/\gamma$ into Eqs. (6)–(9), one can easily obtain

$$\frac{\partial}{\partial\Gamma}\begin{pmatrix}\xi_1\\ \xi_2\\ \xi_3\\ \xi_4\end{pmatrix} = 2\begin{pmatrix}-\xi_2\xi_3\xi_4\\ -\xi_1\xi_3\xi_4\\ \xi_1\xi_2\xi_4\\ \xi_1\xi_2\xi_3\end{pmatrix}\sin\theta_3, \tag{10}$$

with the Manley-Rowe relations [9]

$$\begin{pmatrix}x_1\\ x_2\\ x_3\end{pmatrix} = \begin{pmatrix}\xi_1^2 + \xi_4^2\\ \xi_2^2 + \xi_4^2\\ \xi_3^2 - \xi_4^2\end{pmatrix}, \tag{11}$$

where the constant x_1, x_2 and x_3 are determined by the initial wave amplitude ξ_j (j = 1, 2, 3, 4). The relative phase difference θ_3 [9] is determined by

$$\frac{\mathrm{d}\theta_3}{\mathrm{d}\Gamma} = \kappa_3 + (\xi_1^2 + \xi_2^2 - \xi_3^2 - \xi_4^2) + c\tan\theta_3 \frac{\mathrm{d}}{\mathrm{d}\Gamma}\ln(\xi_1\xi_2\xi_3\xi_4). \tag{12}$$

The system governed by Eqs. (6)–(9), besides the conserving total power (see Eq. (11)), admits of the following additional invariant, namely Hamiltonian,

$$H(\eta,\theta_3) = -4\sqrt{(x_1-\eta)(x_2-\eta)(x_3+\eta)\eta}\cos\theta_3 - \kappa_3\eta + \frac{1}{2}[(x_1-\eta)^2 + (x_2-\eta)^2 + (x_3+\eta)^2 + \eta^2]. \tag{13}$$

Hence, Hamilton system equations explicitly read as

$$\dot{\eta} = \frac{\partial\eta}{\partial\Gamma} = \frac{\partial H}{\partial\theta_3} = 4\sqrt{(x_1-\eta)(x_2-\eta)(x_3+\eta)\eta}\sin\theta_3, \tag{14}$$

$$\dot{\theta}_3 = \frac{\partial\theta_3}{\partial\Gamma} = -\frac{\partial H}{\partial\eta} = 2\cos\theta_3 \cdot \frac{\eta(\eta+x_3)(2\eta-x_1-x_2) + (x_1-\eta)(x_2-\eta)(2\eta+x_3)}{\sqrt{(x_1-\eta)(x_2-\eta)(x_3+\eta)\eta}} + \kappa_3 - (4\eta - x_1 - x_2 + x_3). \tag{15}$$

Equations (6)–(9) reduce to a simplified form, namely one-dimensional Hamilton system, as shown in Eqs. (14) and (15). The advantage of this simplification, concerning

on the topology of the phase-space orbit, gives us an insight into the properties of energy exchange among waves, which controls the stability characteristic of a nonlinear system. Furthermore, the property of equilibrium points (also called singular points or fixed points) can be readily investigated by exploiting the well-developed theory for Hamilton system.

3.1 Phase-space analysis for equal-amplitude sidebands

In this case, the injected wave power is regulated by Mode C, and the condition of $P_1 = P_2$ should be strictly satisfied, which gives rise to the generation of equal-power sidebands. To simplify the calculation, supposing $x_1 = x_2 = 1$ and $x_3 = 0$, Eqs. (14) and (15) are transformed into

$$\dot{\eta} = \frac{\partial H}{\partial \theta_3} = 4(1-\eta)\eta\sin\theta_3, \tag{16}$$

$$\begin{aligned}\dot{\theta}_3 &= -\frac{\partial H}{\partial \eta} \\ &= (2\cos\theta_3 + 1)(2-4\eta) + \kappa_3.\end{aligned} \tag{17}$$

To best unveil the stability characteristic of Hamilton system, one can transform Eqs. (16) and (17) into the form under the rectangular coordinate,

$$\dot{x} = y(4\sqrt{x^2+y^2} + 4x - 2 - \kappa_3), \tag{18}$$

$$\dot{y} = 4(1-x)\sqrt{x^2+y^2} - 8x^2 - 4y^2 + (2+\kappa_3)x, \tag{19}$$

where

$$x = \eta\cos\theta_3,\ y = \eta\sin\theta_3.$$

Moreover, the Jacobi matrix is available from Eqs. (18) and (19):

$$\boldsymbol{J} = \begin{bmatrix} 4y\left(\dfrac{x}{\sqrt{x^2+y^2}} + 1\right) & \dfrac{4(x^2+2y^2)}{\sqrt{x^2+y^2}} + 4x - 2 - \kappa_3 \\ \dfrac{4x-8x^2-4y^2}{\sqrt{x^2+y^2}} - 16x + 2 + \kappa_3 & 4y\left(\dfrac{1-x}{\sqrt{x^2+y^2}} - 2\right) \end{bmatrix}. \tag{20}$$

From Eqs. (18) and (19), one can also explicitly yield a valuable equation describing the phase-space characteristics,

$$\begin{aligned}C = {} & x(1-\sqrt{x^2+y^2}) - \frac{x^2+y^2}{2} \\ & + \frac{(\kappa_3+2)\sqrt{x^2+y^2}}{4},\end{aligned} \tag{21}$$

where C is a constant, dependent seriously on the boundary condition of the system, and Eq. (21) depicts the characteristic of phase-space portraits. The topology of phase-space orbits is significantly affected by the characteristic of singular point, which makes a significant influence to the stabilization of the system. From Eqs. (18) and (19), one can easily obtain singular points for the following four different types:

1) $(x, y) = ((\kappa_3 + 6)/12, 0)$. Remarkably, the liner-phase-mismatch profile should satisfy the condition of $\kappa_3 > -6$. Furthermore, one can get the eigenvalue equation: $\lambda^2 = (\kappa_3 + 6)(\kappa_3 - 6)/3$. If κ_3 lies in the interval of $(-6, 6)$, the singular point will turn out to be a center point; otherwise, if κ_3 is in the range of $(6, +\infty)$, the singular point will be a saddle point, and they are both controlled by the characteristic of eigenvalue [10].

2) $(x, y) = ((\kappa_3 - 2)/4, 0)$. Based on the similar principal, the eigenvalue equation can be yielded with $\lambda^2 = (\kappa_3 + 2)(\kappa_3 - 2)$, under the condition of $\kappa_3 < 2$. Notably, the singular point will be a center point as long as $-2 < \kappa_3 < 2$; otherwise, the singular point will be turned into a saddle point if $\kappa_3 < -2$.

3) $(x, y) = (0, 0)$. This specially fixed point resides in the liner-phase-mismatch condition of $\kappa_3 \in (-\infty, -6) \cup (2, +\infty)$, characterized by the eigenvalue equation $\lambda^2 = -(\kappa_3 + 2)^2$, and it will be definitely the center point.

4) $(x,y) = \left((\kappa_3 - 2)/4, \pm\sqrt{12 - \kappa_3^2 + 4\kappa_3}/4\right)$. Interesting is that the condition for the existence of this type singular point is $-2 < \kappa_3 < 6$, and the fixed point will be nothing but a saddle point. This conclusion is drawn by analyzing the characteristics of the eigenvalue equation of $\lambda^2 = -(\kappa_3 + 2)(\kappa_3 - 6)$.

Consider the anomalous-dispersion regime first. Figures 2(a) and 2(b) display phase-space portraits with $\kappa_3 = -7$ and $\kappa_3 = -3$, describing FWM dynamics, and one can clearly see that phase-space portraits contain only one center point, around which the representative point of the field moves on stable periodic trajectories in the physical limits regime, and thus the sideband wave varies in a stable mode. The fact that, κ_3 with a relatively large value leads to a small periodic exchange of energy between the injected and sideband waves, is demonstrated in our case. Moreover, out of the physical limits regime, the unstable saddle point, which would be present when two eigensolutions exchange their stability, does not assume the physical significance.

Figure 2(c) shows a completely different scenario when κ_3 is increased up to $\kappa_3 = -1$. In fact, when $\kappa_3 = -2$ (referred to Fig. 3(a)), the exchange of stability between eigensolutions is a standard characteristic exhibiting the transcritical bifurcation, in which the original stable mode

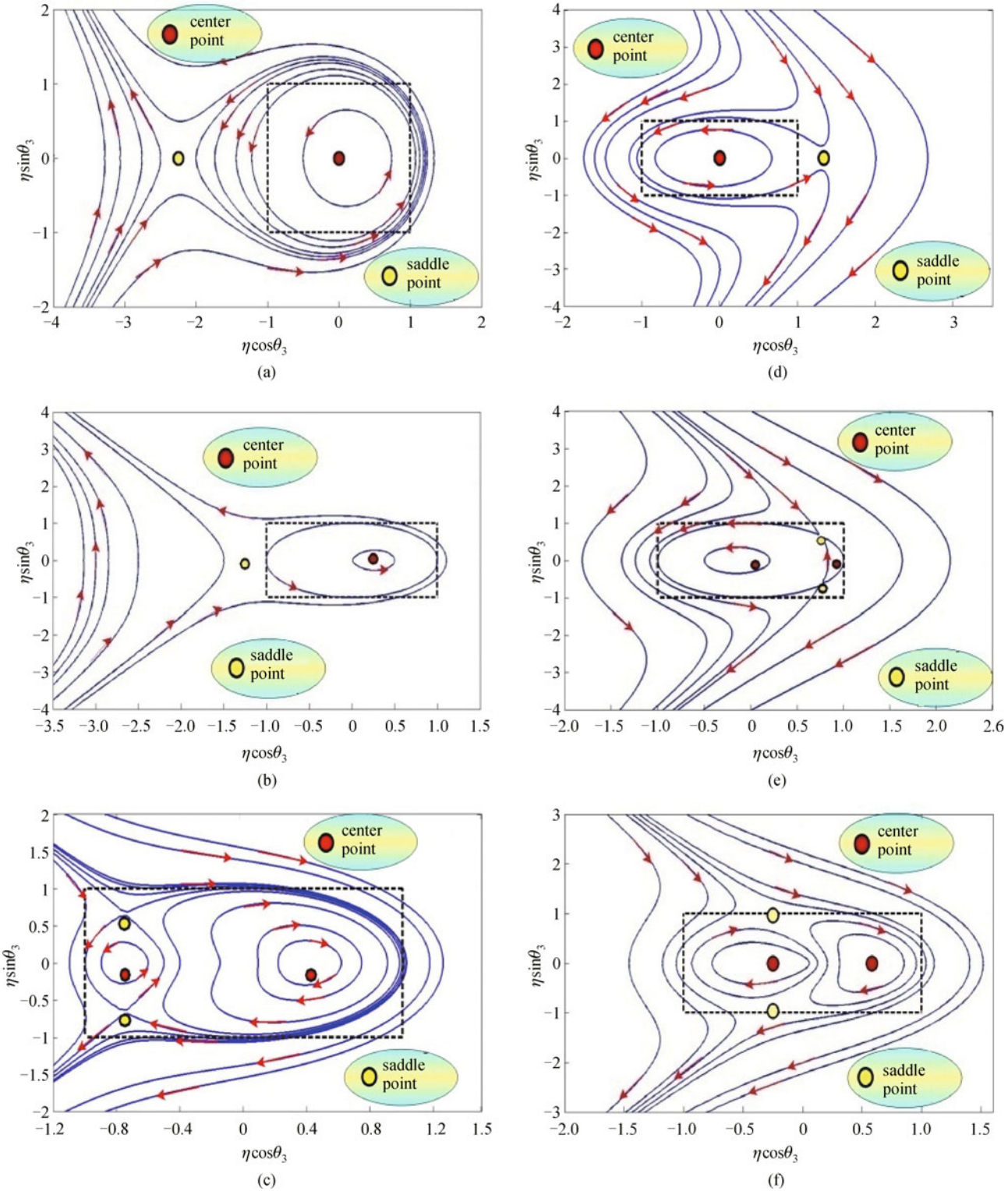

Fig. 2 Phase-space portraits with abnormal dispersion (see (a), (b) and (c)) and normal dispersion (see (d), (e) and (f)) regimes. (a) $\kappa_3 = -7$; (b) $\kappa_3 = -3$; (c) $\kappa_3 = -1$; (d) $\kappa_3 = 10$; (e) $\kappa_3 = 5$; (f) $\kappa_3 = 1$. Physical limits require that $-1 \leqslant \eta\cos\theta_3 \leqslant 1$ and $-1 \leqslant \eta\sin\theta_3 \leqslant 1$

vanishes, accompanied with the emergence of two newly central points (stable mode) and two newly saddle points (unstable mode). Moreover, if the representative point moves around the saddle point, the energy can be significantly coupled from the injected to sideband wave. As for two saddle points in Fig. 2(c), it is clearly found that they simultaneously have both the stable and unstable characteristics. On the one hand, the arrow on the

trajectory points to the equilibrium point marked with yellow color, featuring the stability characteristic; on the other hand, the arrow, deviating from the above equilibrium point, points to another equilibrium point, exhibiting the unstable characteristic for the first equilibrium point. The trajectory that connects two saddle points is named "heteroclinic orbit" and the corresponding equilibrium point is called "heteroclinic point." As seen in Fig. 2(c), the spatial instability of sidebands entails that power exchange from the injected to sideband waves is greatly enhanced. Remarkably, the spatial period of the conversion diverges to infinity on the loop heteroclinic separatrix that stems from the saddle points at $(-3/4, \pm\sqrt{7}/4)$.

Going on increasing the value of κ_3 up to the normal-dispersion regime, it is found that the topology of phase-space orbits retains invariable, until κ_3 is increased up to $\kappa_3 = 6$ (see Fig. 3(a)). As shown in Fig. 2(e), phase-space trajectories are also divided into four separated regions, which is similar with Fig. 2(c). Differently, the saddle points are displaced from the left to right half-plane. Interestingly, as alluded earlier, when $\kappa_3 \geqslant 6$, the topology of phase-space orbits is dramatically changed and comprises one stable center point (in the physical limits regime) and one unstable saddle point (out of the physical limits regime), and this characteristic is illustrated in Fig. 2(d) with $\kappa_3 = 10$. In fact, transcritical bifurcation takes place under the condition of $\kappa_3 = 6$.

As illustrated in Fig. 3(a), distribution of singular point I and II implies that $\cos\theta_3$ is proportional to κ_3, and the center and saddle points are marked with circle and asterisk, respectively. Remarkably, the critical point 1 (6, 1) and point 2 $(-2, -1)$ simultaneously have both the stable and unstable characteristics, and the singular point IV, expressed as $(x,y)=\left((\kappa_3-2)/4, \pm\sqrt{12-\kappa_3^2+4\kappa_3}/4\right)$, varies with κ_3 in a nonlinear manner, and it travels along with two different routes, marked with different colors in Fig. 3(b). Remarkably, the projection of 3D plot at x-y plane is just a perfect circle, which implies that the representative point moves on a circle orbit. Finally, the equilibrium point (0, 0) will survive under the condition of $\kappa_3 \in (-\infty, -6)\cup(2, +\infty)$, and one can safely obtain the conclusion that if the representative point moves on a circle orbit around the point (0, 0), energy exchange between the injected and sideband waves is small.

3.2 Phase-space analysis for approximate-equal-amplitude sidebands

An assumption of $x_1 = 1$ and $x_2 \approx 1$ with $x_3 = \alpha \approx 0$ is made in this section, referred to the case for approximate-equal-amplitude sidebands. Strictly speaking, Mode C survives under the boundary condition of $x_1 = x_2 = 1$ and $x_3 = 0$, but for $x_2 \approx 1$, Mode C also plays a dominate role in MFWM processes. One can easily get the following equations from Eqs. (14) and (15) with

$$\dot{\eta} = 4(1-\eta)\sqrt{\eta(\alpha+\eta)}\sin\theta_3, \tag{22}$$

$$\begin{aligned}\dot{\theta}_3 =& 2\cos\theta_3 \\ &\cdot\left[-2\sqrt{\eta(\alpha+\eta)} + (1-\eta)\left(\sqrt{\frac{\alpha+\eta}{\eta}} + \sqrt{\frac{\eta}{\alpha+\eta}}\right)\right] \\ &+ \kappa_3 + 2 - 4\eta - \alpha.\end{aligned} \tag{23}$$

Equations (22) and (23) can be adopted to analyze a conserved Hamilton system describing Mode C. For the sake of simplicity, we can analyze the Hamilton system under the polar coordinate with the Jocabi matrix given by

$$\boldsymbol{J} = \begin{bmatrix} -\dfrac{8\eta^2 + (6\alpha-4)\eta - 2\alpha}{\sqrt{(\eta+\alpha)\eta}}\sin\theta_3 & 4(1-\eta)\sqrt{\dfrac{\eta+\alpha}{\eta}}\cos\theta_3 \\ \dfrac{\alpha^2(\eta-1) - 4\eta(\eta+\alpha)(2\eta+\alpha)}{\sqrt{[(\eta+\alpha)\eta]^3}}\cos\theta_3 - 4 & \dfrac{8\eta^2 + (6\alpha-4)\eta - 2\alpha}{\eta\sqrt{(\eta+\alpha)\eta}}\sin\theta_3 \end{bmatrix}. \tag{24}$$

The relation of x and y can be explicitly yielded from Eqs. (22) and (23):

$$\begin{aligned}C =& x(1-\sqrt{x^2+y^2})\sqrt{1+\frac{\alpha}{\sqrt{x^2+y^2}}} - \frac{x^2+y^2}{2} \\ &+ \frac{(\kappa_3+2-\alpha)\sqrt{x^2+y^2}}{4},\end{aligned} \tag{25}$$

where C, x and y have been defined in Eq. (21). Remarkably, Eq. (25) can be degenerated into Eq. (21) if $\alpha = 0$. Similarly, the stable points for Eqs. (22) and (23) can be classified as the following two aspects:

1) $(\eta, \theta_3) = \left(1, \cos^{-1}[(\kappa_3-2-\alpha)/(4\sqrt{1+\alpha})]\right)$ or $\left(1, 2\pi - \cos^{-1}[(\kappa_3-2-\alpha)/(4\sqrt{1+\alpha})]\right)$. The fixed point, given by $(x, y) = \left((\kappa_3-2-\alpha)/(4\sqrt{1+\alpha}), \pm\sqrt{1-(\kappa_3-2-\alpha)^2/16(1+\alpha)}\right)$ under the rectangle coordinate, will exist under the condition of $\kappa_3 \in (2+\alpha-4\sqrt{1+\alpha}, 2+\alpha+4\sqrt{1+\alpha})$. Furthermore, one can easily obtain the eigenvalue with $\lambda_{1,2} = \pm\sqrt{16(1+\alpha)-(\kappa_3-2-\alpha)^2}$, which implies that the fixed point will be definitely an unstable saddle point.

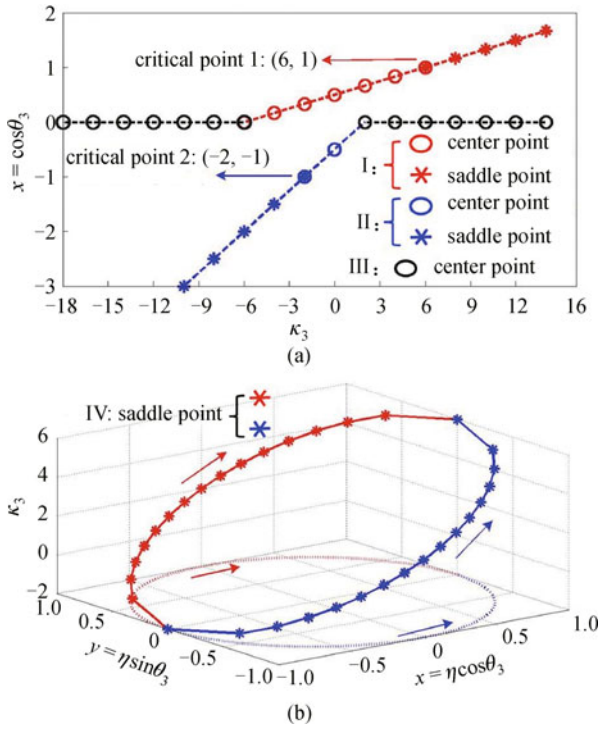

Fig. 3 Illustration of distribution of singular points with different values of κ_3. (a) Plot for singular point I $(x, y) = ((\kappa_3 + 6)/12, 0)$, singular point II $(x, y) = ((\kappa_3 - 2)/4, 0)$ and singular point III $(x, y) = (0, 0)$; (b) plot for singular point IV $(x,y) = \left((\kappa_3 - 2)/4, \pm\sqrt{12 - \kappa_3^2 + 4\kappa_3}/4\right)$

2) $(\eta, \theta_3) = (\eta_0, \pi)$ or $(\eta_0, 2\pi)$. η_0 is the root of the following equation:

$$\eta^4 + a\eta^3 + b\eta^2 + c\eta + d = 0, \tag{26}$$

where

$a = (9\alpha + \kappa_3 - 6)/6$,

$b = [27\alpha^2 + 10(\kappa_3 - 6)\alpha + 12 - 4\kappa_3 - \kappa_3^2]/48$,

$c = [-\alpha^3 + 2(\kappa_3 - 10)\,\alpha^2 + (12 - 4\kappa_3 - \kappa_3^2)/48]$,

$d = \alpha^2/12$.

The eigenvalue equation for this case is

$$\lambda^2 = 8\left(1 - \frac{1}{\eta}\right)\left[2\eta + \alpha + \left(\sqrt{\eta + \alpha} \mp \sqrt{\eta}\right)^2 + \frac{\alpha^2(1 - \eta)}{2(\eta + \alpha)\eta}\right]. \tag{27}$$

By substituting the root η_0 of Eq. (26) into Eq. (27), the eigenvalue λ can be thus obtained, and we can further judge the type of a singular point that if $0 < \eta_0 < 1$, it will be a center point; otherwise, it will turn to be a saddle point. Under the rectangle coordinate, the corresponsive fixed points are $(x, y) = (\pm \eta_0, 0)$, which implies that the fixed points appear at x-axis and are located symmetrically in terms of y-axis.

Figure 4 depicts distribution of singular points when taking account of $\alpha = 0.01$. As mentioned before, firstly, the point $(x,y) = \left((\kappa_3 - 2 - \alpha)/(4\sqrt{1 + \alpha}), \pm\sqrt{1 - (\kappa_3 - 2 - \alpha)^2/16(1 + \alpha)}\right)$ satisfies the relation of $x^2 + y^2 = 1$, which represents that it moves on a circle trajectory, as shown in Fig. 4(a). It is worthy noting that when $\kappa_3 = 3.5$, two saddle points P_3 (0.3725, 0.928) and P_4 (0.3725, −0.928) can be obtained, corresponding to yellow points in Fig. 5(b). Secondly, singular points $(x, y) = (\pm\eta_0, 0)$ are illustrated in Fig. 4(b), and interesting is that κ_3 varies with η in a linear manner, but in different directions. Moreover, two critical points, provided with both the stable and unstable characteristics, are identified to (1, 6.03) and (1, −2.01).

Figure 5 illustrates phase-space portraits with $\kappa_3 = -3$, $\kappa_3 = 3.5$ and $\kappa_3 = 7$, respectively. From what has been discussed above, we know that $\kappa_3 = -2.01$ and $\kappa_3 = 6.03$ are two critical linear-phase-mismatch values that dramatically change the topology structure of phase-space trajectories, and that further influence energy exchange among the waves. As shown in Figs. 5 (a) and 5(c), the saddle point shifts from the left to right half-plane for phase-space orbits, with respect to the center point, during which the number of saddle point is also increased up to two, as seen in Fig. 5(b).

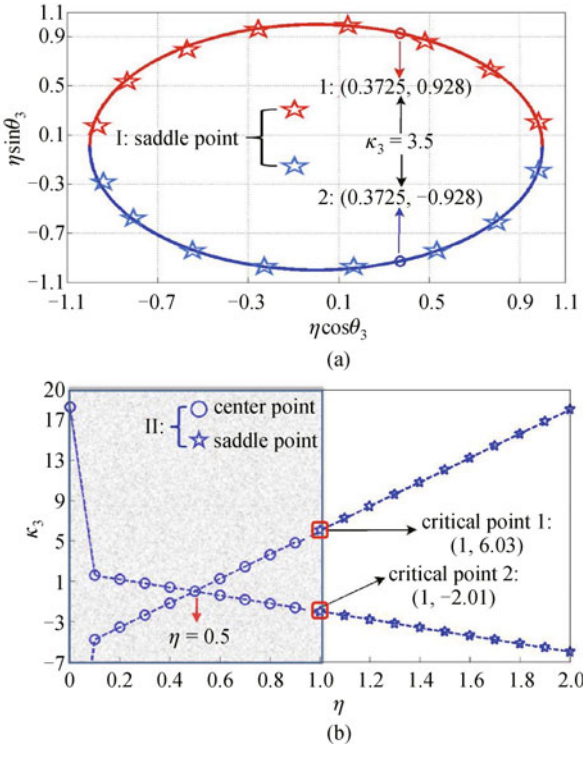

Fig. 4 Illustration of distribution of singular points with different values of κ_3. (a) Plot for singular point $(x,y) = ((\kappa_3 - 2 - \alpha)/(4\sqrt{1 + \alpha}), \pm\sqrt{1 - (\kappa_3 - 2 - \alpha)^2/[16(1 + \alpha)]})$; (b) plot for singular point $(x, y) = (\pm\eta_0, 0)$

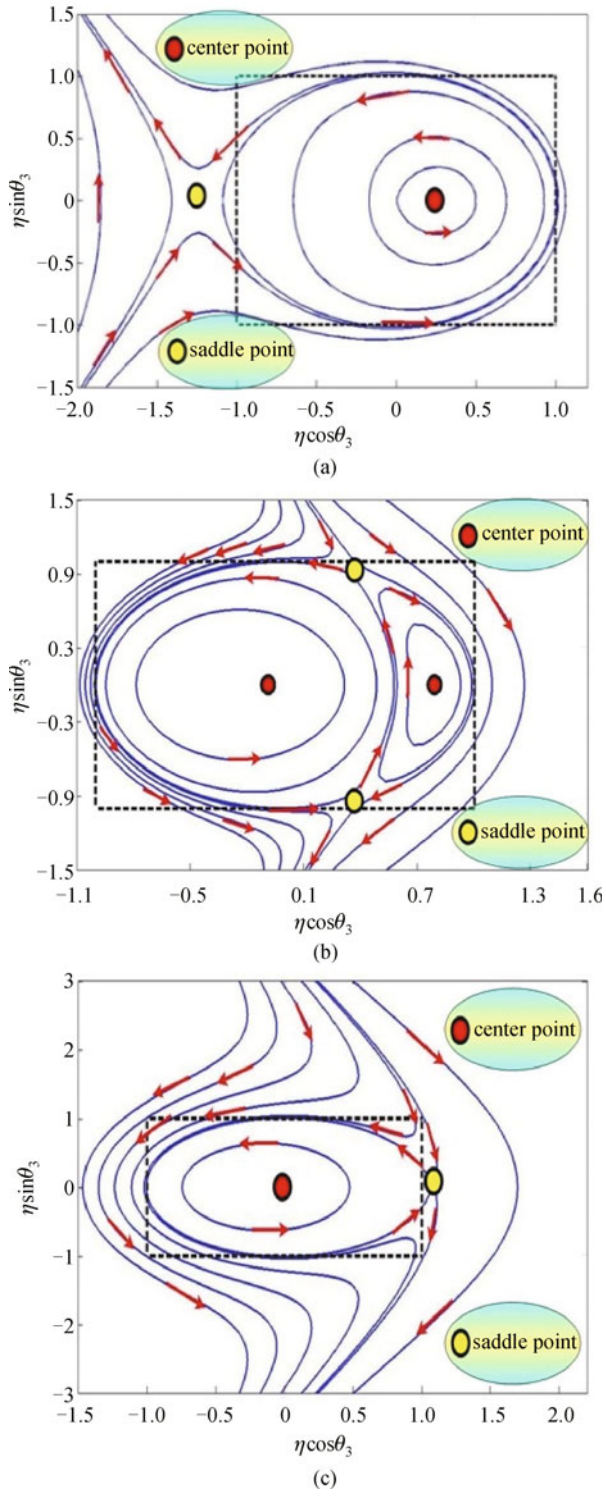

Fig. 5 Illustration for phase-space portraits with (a) $\kappa_3 = -3$; (b) $\kappa_3 = 3.5$ and (c) $\kappa_3 = 7$. Physical limits require that $-1 \leqslant \eta\cos\theta_3 \leqslant 1$ and $-1 \leqslant \eta\sin\theta_3 \leqslant 1$

Figure 6(a) illustrates sideband power as a function of Γ when κ_3 varies from -5 to 5. As long as κ_3 increases approximately from -2.5 to 0.5, intense interaction between the injected and sideband wave takes place, and the sideband wave can obtain high energy from the injected wave. In addition, projection of Fig. 6(a) at η-κ_3 plane is also displayed in the inset of Fig. 6(b), and the red curve in Fig. 6(b) indicates fractional power loss (FPL) for the injected wave as a function of κ_3, which can be also regarded as the envelope of the inset. Here, FPL is defined as $\eta/1 \times 100\%$, reflecting power attenuation of the injected wave. It is expected that FPL will exceed 50% when κ_3 ranges from -2.4 to 0.4, implying the occurance of a dramatic energy exchange between the injected and sideband waves. Furthermore, a FPL of about 100% can be attained if $\kappa_3 \approx -0.4$, and then almost all the injected wave power is delivered to the sideband wave.

To further unveil the relation between phase-space orbit and power exchange among the waves, we explicitly mimic and compare phase-space orbits, η vs. Γ curve and $\cos\theta_3$ vs. Γ curve, under the condition of $\kappa_3 = -1$ and $\kappa_3 = 4$, corresponding to unstable and stable modes, as shown in Fig. 7. Especially, Fig. 7(a) illustrates unstable phase-space orbits, on which the representative point moves in a larger range than that shown in Fig. 7(d). η vs. Γ curve in Fig. 7(b) indicates that the sideband wave can obtain approximate 80% injected-wave power, which is much larger than that shown in Fig. 7(e) and the sideband wave power in Fig. 7(b) varies with Γ periodically with its period almost four times larger than that shown in Fig. 7(e). On

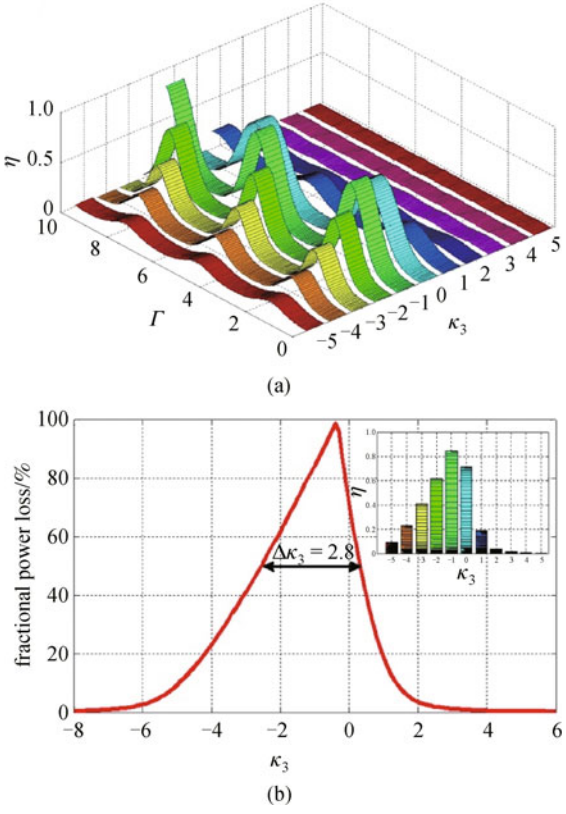

Fig. 6 (a) Sideband power as a function of Γ with different values of κ_3; (b) fractional power loss as a function of κ_3

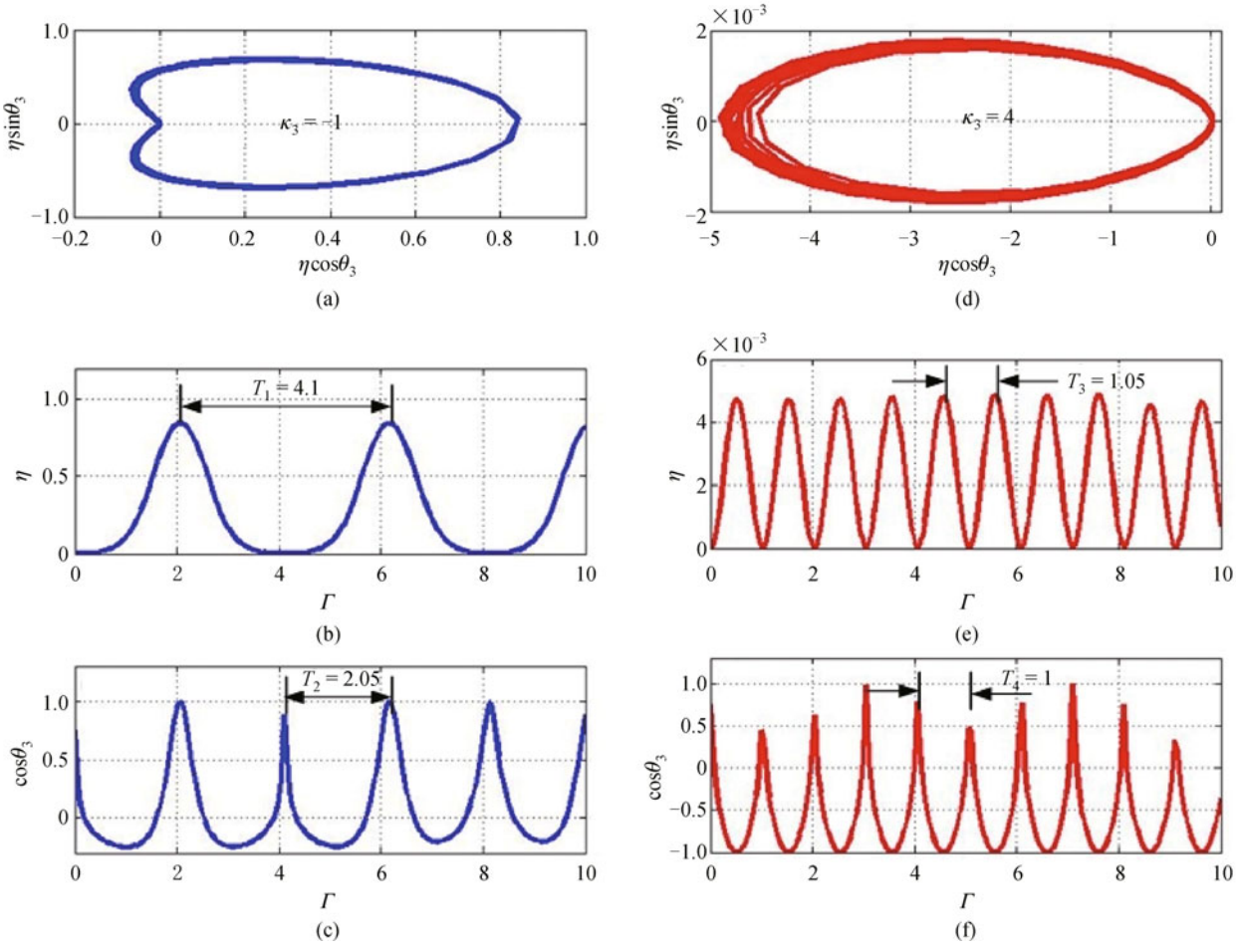

Fig. 7 Illustration of phase-space trajectories representing (a) an unstable saddle point with $\kappa_3 = -1$ and (d) a stable center point with $\kappa_3 = 4$. η vs. Γ with (b) $\kappa_3 = -1$ and (e) $\kappa_3 = 4$. $\cos\theta_3$ vs. Γ with (c) $\kappa_3 = -1$ and (f) $\kappa_3 = 4$

another perspective, a large period for η vs. Γ curve is benefit to energy accumulation when the sideband wave propagating along an optical fiber, and the amount of period is significantly dependent on $\cos\theta_3$ vs. Γ curve, which in facet reflects the varying rate of power for the sideband wave. The varying rate for $\cos\theta_3$ vs. Γ curve in Fig. 7(c) is much slower than that in Fig. 7(f), and this characteristic can be adopted to explain the phenomena in Figs. 7(b) and 7(e).

3.3 Analysis for Hamilton system

Through using simultaneous Eqs. (14) and (15), and taking account of the initial conditions of $x_1 = x_2 = 1$ and $x_3 = 0$, one can obtain

$$\dot{\eta} = \Theta \cdot \sqrt{f(\eta)}, \tag{28}$$

with

$$f(\eta) = \eta^4 + [(\kappa_3 - 6)/3]\eta^3 + \{[12 + 4H - (\kappa_3 + 2)^2)]/12\}\eta^2 + [(1-H)(\kappa_3 + 2)/6]\eta - (H-1)^2/12$$

and $\Theta = \pm 2\sqrt{3}$. Equation (28) can be well explained as an evolution equation for the velocity of an ideal point moving in a potential well $V(\eta)$ with a totally conserved energy E, which may be integrated to yield the solution in an implicit form,

$$\Gamma = \frac{1}{\Theta}\int_{\eta(\Gamma=0)}^{\eta(\Gamma=\mathrm{L})} \frac{1}{\sqrt{f(\eta)}} \mathrm{d}\eta = \frac{1}{\Theta}\int_{\eta(\Gamma=0)}^{\eta(\Gamma=\mathrm{L})} \frac{1}{\sqrt{2[E - V(\eta)]}} \mathrm{d}\eta, \tag{29}$$

with the potential well explicitly reading as

$$V(\eta) = -\int_0^{\eta} \frac{\partial^2 \eta}{\partial \Gamma^2} \mathrm{d}\eta = -\left[\frac{f(\eta)}{2} + \frac{(H-1)^2}{24}\right], \tag{30}$$

and the totally conserved energy

$$E = \frac{1}{2}\dot{\eta}^2 + V(\eta) = -\frac{(H-1)^2}{24} \tag{31}$$

is uniquely characterized by the initial settings for H and

κ_3. Γ can be explicitly yielded from Eq. (29) with the form of periodic Jacobi elliptic and hyperbolic function [10]. The form of the solution for Γ presumably depends on the root of the fourth-order polynomial $f(\eta)$.

Potential well is a key parameter that can estimate the capability of power exchange among waves in a conserved Hamilton system, and it also influences the characteristic of a singular point and the topology of phase-space orbits. Figure 8(a) illustrates potential well energy $V(\eta)$ vs. normalized power η with $H = 1$ and different values of κ_3, and all the concave points, namely stable equilibrium points, are assembled to form curve 1 in Fig. 8(a). What's more, stable eigensolutions are available from curve 1, which are increased with the decrement of κ_3. Conversely, all the salient points in Fig. 8(a), assembled to form curve 2, corresponds to unstable equilibrium points, and they are decreased with the decrement of κ_3. Figure 8(b) further illustrates potential well energy $V(\eta)$ vs. normalized power η with $\kappa_3 = 1$ and different values of H. Notably, different values of H denote different initial conditions for injected waves, and stable equilibrium points with $\eta = 0.5$ will be turned into unstable equilibrium points if H increases from < 2.5 to > 2.5 (see curve 2), where $H = 2.5$ is the critical point marked with five-pointed star in Fig. 8(b). Curve 1 in Fig. 8(b) is the aggregation of salient points, which does not assume physical significance. Simulation for potential well energy as a function of η and κ_3 with $H = 1$ has been implemented, as shown in Fig. 8(c), which intuitively illustrates the evolution of stable (green line) and unstable (black and red lines) equilibrium evolves with the increment of κ_3.

To obtain the extreme points, one should find the roots from the following third-order polynomial equation

$$\frac{\partial V(\eta)}{\partial \eta} = -\frac{1}{2}\left[4\eta^3 + (\kappa_3 - 6)\eta^2 + \frac{12 + 4H - (\kappa_3 + 2)^2}{6}\eta + \frac{(1-H)(\kappa_3 + 2)}{6}\right] = 0, \tag{32}$$

and the roots can be analytically obtained as follows:

$$\eta_j = y_j - e/3, \ (j = 1,2,3), \tag{33}$$

with

$$\begin{cases} y_1 = \sqrt[3]{T + \sqrt{D}} + \sqrt[3]{T - \sqrt{D}}, \\ y_2 = m_1 \sqrt[3]{T + \sqrt{D}} + m_2 \sqrt[3]{T - \sqrt{D}}, \\ y_3 = m_2 \sqrt[3]{T + \sqrt{D}} + m_1 \sqrt[3]{T - \sqrt{D}}. \end{cases} \tag{34}$$

Here,

$e = (\kappa_3 - 6)/4$, $D = (q/2)^2 + (p/3)^3$,
$f = [12 + 4H - (\kappa_3 + 2)^2]/24$, $g = (\kappa_3 + 2)(1 - H)/24$,
$T = -q/2$, $p = f - e^2/3$, $q = 2e^3/27 - ef/3 + g$,
$m_1 = (-1 + \sqrt{3}i)/2$,
$m_2 = (-1 - \sqrt{3}i)/2$.

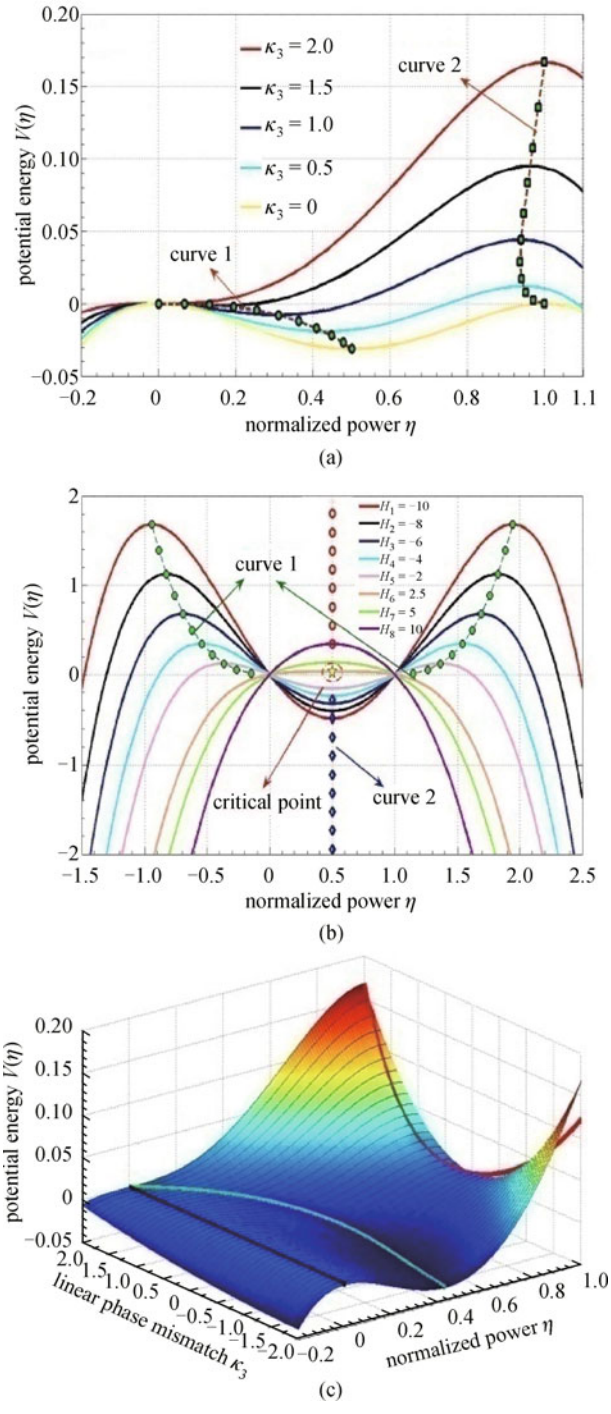

Fig. 8 (a) Potential well energy $V(\eta)$ vs. normalized power η with $H = 1$ and different values of κ_3; (b) potential well energy $V(\eta)$ vs. normalized power η with $\kappa_3 = 1$ and different values of Hamiltonian parameter H; (c) 3D plot for potential well energy $V(\eta)$ as function of normalized power η and linear phase mismatch κ_3 when $H = 1$. Physical limits require that $0 \leqslant \eta \leqslant 1$

The complex root implies that there is no extreme point in potential well curve. Therefore, we can discuss the property of the roots in Eq. (34) from the following three aspects:

1) If $D > 0$, there is only one real root (y_1) and two conjugated complex roots (y_2 and y_3), and thus there is only one equilibrium point in $V(\eta)$ vs. η curve.

2) If $D < 0$, the roots obtained are all real number, and hence there are three equilibrium points in $V(\eta)$ vs. η curve.

3) If $D = 0$ and $p = q = 0$, the three roots are identified with $\eta_{1,2,3} = -e/3$, corresponding to only one equilibrium point in $V(\eta)$ vs. η curve; if $D = 0$ and $(q/2)^2 = -(p/3)^3 \neq 0$, the roots are $\eta_1 = 2\sqrt[3]{T} - e/3$, and $\eta_{2,3} = -\sqrt[3]{T} - e/3$, corresponding to two equilibrium points in $V(\eta)$ vs. η curve.

From what has been discussed above, the equilibrium point in potential well curve can be robustly governed by κ_3 and H, which would further influence energy exchange between the injected and sideband waves.

4 Characteristic of satellite

Satellite wave is one of the sideband waves with angular frequency ω_4, which is adjacent to the injected wave with angular frequency ω_2 and is phase conjugated to the injected wave with angular frequency ω_1, as seen in Fig. 1. Figure 9(a) displays the well known Young's double-slit experiment based on two coherent waves interfering with each other, in which the two waves experience different optical paths and thus form alternatively light (green line) and dark (black line) fringes. A similar phenomenon also takes place when satellite wave travels over an optical fiber, originated from the MFWM effect, as shown in Fig. 9(b), and the sameness and difference of the two phenomena are demonstrated in detail in Table 2.

Supposing $|A_1| > |A_2| >> |A_3| > |A_4|$, $|A_1(z)| \approx |A_1(0)|$ and $|A_2(z)| \approx |A_2(0)|$, the satellite-wave amplitude can be explicitly derived from Eqs. (1)–(4),

$$A_4(z) \approx \frac{2\gamma^2 P_1^{\frac{3}{2}} P_2}{(3\gamma P_2 - \Delta\beta_1)} \times \left\{ \frac{\exp[\mathrm{i}(3\gamma P_1 + \Delta\beta_1 - \Delta\beta_3)z] - 1}{3\gamma P_1 + \Delta\beta_1 - \Delta\beta_3} - \frac{\exp[\mathrm{i}(3\gamma P_1 + 3\gamma P_2 - \Delta\beta_1)z] - 1}{3\gamma P_1 + 3\gamma P_2 - \Delta\beta_1} \right\} + \gamma P_2 \sqrt{P_1} \times \frac{\exp[\mathrm{i}(3\gamma P_1 - \Delta\beta_2)z] - 1}{3\gamma P_1 - \Delta\beta_2}. \quad (35)$$

The solution indicated in Eq. (35) is improved a lot compared to the result reported in Ref. [9], whose authors do not consider the impact of idler wave on satellite wave. Since satellite wave is a second-order FWM product, the impact of idler wave on satellite wave cannot be ignored. The big bracket in Eq. (35) indicates that pump, signal and idler waves together contribute to the amplitude of satellite wave. The satellite-wave power can be yielded from

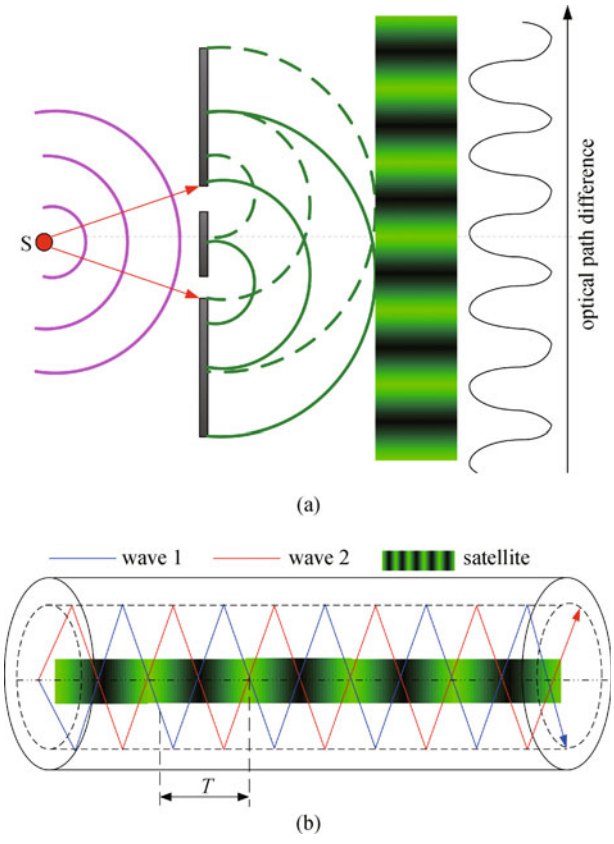

Fig. 9 (a) Comparison of Young's double-slit experiment and (b) evolvement of satellite wave over an optical fiber

Eq. (35),

$$P_4 = |A_4|^2 \approx \frac{4m^2}{a^2}\sin^2\left(\frac{az}{2}\right) + \frac{4m^2}{b^2}\sin^2\left(\frac{bz}{2}\right) + \frac{4m^2}{c^2} \cdot \sin^2\left(\frac{cz}{2}\right) - \frac{8m^2}{ab}\sin\left(\frac{az}{2}\right)\sin\left(\frac{bz}{2}\right)\cos\left[\frac{(a-b)z}{2}\right] + \frac{8mn}{ac}\sin\left(\frac{az}{2}\right)\sin\left(\frac{cz}{2}\right)\cos\left[\frac{(a-c)z}{2}\right] - \frac{8mn}{bc} \cdot \sin\left(\frac{bz}{2}\right)\sin\left(\frac{cz}{2}\right)\cos\left[\frac{(b-c)z}{2}\right] \quad (36)$$

with

$$\begin{cases} m = 2\gamma^2 P_1^{\frac{3}{2}} P_2/(3\gamma P_2 - \Delta\beta_1), n = \gamma P_2 \sqrt{P_1}, \\ a = 3\gamma P_1 + \Delta\beta_1 - \Delta\beta_3, \\ b = 3\gamma P_1 + 3\gamma P_2 - \Delta\beta_1, \\ c = 3\gamma P_1 - \Delta\beta_2. \end{cases} \quad (37)$$

Table 2 Comparison of Young's double-slit experiment and evolvement of satellite wave over an optical fiber

	Young's double-slit experiment	evolvement of satellite wave
sameness	alternatively bright and dark fringes	
	need of two injected waves	
	related to phase difference of two injected waves	
	polarization dependence of two injected waves	
difference	need of two coherent waves	free of coherent characteristic for the two waves
	injected waves with a uniform wavelength	injected waves with different wavelengths
	distribution of fringes depending on the injected wavelength and dimensional structure of the experimental installation	distribution of fringes depending on the injected wavelengths and powers
	no new component generation	new component generation
	non-essential of optical fiber	need of optical fiber

Note that $\Delta\beta_1 + \Delta\beta_2 + \Delta\beta_3 = 0$, and it leads to the result of $a = c$. Thus, Eq. (36) can be further simplified with

$$P_4 \approx \frac{4(m+n)^2}{a^2}\sin^2\left(\frac{az}{2}\right) + \frac{4m^2}{b^2}\sin^2\left(\frac{bz}{2}\right) - \frac{8m(m+n)}{ab} \cdot \sin\left(\frac{az}{2}\right)\sin\left(\frac{bz}{2}\right)\cos\left[\frac{(a-b)z}{2}\right]. \tag{38}$$

The extreme points yielded from Eq. (38) are

$$P_4 \approx \begin{cases} 4\left[\frac{m+n}{a}\sin\left(\frac{2al}{a-b}\pi\right) - \frac{m}{b}\sin\left(\frac{2bl}{a-b}\pi\right)\right]^2, & \frac{a-b}{2}z = 2l\pi, \\ 4\left\{\frac{m+n}{a}\sin\left[\frac{a(2l+1)}{a-b}\pi\right] + \frac{m}{b}\sin\left[\frac{b(2l+1)}{a-b}\pi\right]\right\}^2, & \frac{a-b}{2}z = (2l+1)\pi, \quad l \in Z. \\ \frac{4(m+n)^2}{a^2}\sin^2\left[\frac{a(2l+1)}{2(a-b)}\pi\right] + \frac{4m^2}{b^2}\sin^2\left[\frac{b(2l+1)}{2(a-b)}\pi\right], & \frac{a-b}{2}z = \left(l+\frac{1}{2}\right)\pi, \end{cases} \tag{39}$$

To make clear the physical implication of Eq. (39), we define $\Delta\phi = \Delta k \times z = (k_1 - k_2)z = (a - b)z/2$, where Δk represents the difference of different net phase mismatch profiles, and $\Delta\phi$ denotes accumulation of phase-mismatch difference along an optical fiber, which determines the intense of satellite wave. In this case, an assumption that Δk retains invariable and z varies at will is made. At first, when $z = 4l\pi/(a - b)$, $P_4 \approx 4\{[(m + n)/a]\sin[2al\pi/(a - b)] - (m/b)\sin[2bl\pi/(a - b)]\}^2$, and it is remarkable that $2al\pi/(a - b) - 2bl\pi/(a - b) = 2l\pi$, which shows that the two terms $[(m + n)/a]\sin[2al\pi/(a - b)]$ and $(m/b)\sin[2bl\pi/(a - b)]$ are in-phase. Hence, the whole process is identified to a interfered-destructive case, giving rise to a dark fringe emerging at the point of $z = 4l\pi/(a - b)$. Secondly, when $z = 2(2l + 1)\pi/(a - b)$, $P_4 \approx 4\{[(m + n)/a]\sin[a(2l + 1)\pi/(a - b)] + (m/b)\sin[b(2l + 1)\pi/(a - b)]\}^2$. We note that $a(2l + 1)\pi/(a - b) - b(2l + 1)\pi/(a - b) = (2l + 1)\pi$, so the two terms $[(m + n)/a]\sin[a(2l + 1)\pi/(a - b)]$ and $(m/b)\sin[b(2l + 1)\pi/(a - b)]$ are out of phase. This issue, however, also equals to a interfered-destructive case, because of the "+" sign located between the two terms. When $z = (2l + 1)\pi/(a - b)$, $P_4 \approx 4(m + n)^2/a^2\sin^2[a(2l + 1)\pi/(2a - 2b)] + 4m^2/b^2\sin^2[b(2l + 1)\pi/(2a - 2b)]$, which can be further simplified as: $P_4 \approx 2(m + n)^2/a^2 + 2m^2/b^2$, and it is identified to a interfered-constructive term.

Furthermore, Eq. (38) can be transformed into another form, that is

$$P_4 \approx M\cos\left(\frac{2\pi}{T_a}\cdot z\right) + N\cos\left(\frac{2\pi}{T_b}\cdot z\right) + R\cos\left(\frac{2\pi}{T_{a-b}}\cdot z\right) + Q, \tag{40}$$

with

$$\begin{cases} M = \frac{2(m+n)}{a}\left(\frac{m}{b} - \frac{m+n}{a}\right), N = \frac{2m}{b}\left(\frac{m+n}{a} - \frac{m}{b}\right), \\ R = -\frac{2m(m+n)}{ab}, \\ Q = 2\left(\frac{m+n}{a} - \frac{m}{b}\right)^2 + \frac{2m(m+n)}{ab}, \\ T_a = \frac{2\pi}{a}, T_b = \frac{2\pi}{b}, T_{a-b} = \frac{2\pi}{a-b}. \end{cases} \tag{41}$$

Mathematically, Eqs. (40) and (41) point out that the expression for the power of satellite wave can be

approximately regarded as a complex of three cosine functions, and the irregular period T for satellite power vs. fiber length curve is controlled by $|T_a|$, $|T_b|$ and $|T_{a-b}|$, respectively. Note that, T_a, T_b and T_{a-b} are related to a and b, which means that one can adjust the injected wavelength detune to change the irregular period T. Further investigation shows that the irregular period can be yielded through the manipulation of $T = [|T_a|, |T_b|, |T_{a-b}|]$, while the middle bracket denotes the operation of searching the least common multiple in an array.

Figure 10(a) shows the evolvement of satellite wave over an optical fiber, under the condition of $\lambda_1 = 1555$ nm, $\lambda_2 = 1545$ nm, $P_{10} = 20$ mW, $P_{20} = 10$ mW. The red dash line and green dots represent the numerical simulation and the analytical solution, respectively, and they are in high agreement. It can be clearly seen that satellite power varies with fiber length in a sine-like trajectory, in line with the analysis for Eqs. (38) and (39). By changing the boundary condition with $\lambda_1 = 1555$ nm, $\lambda_2 = 1548$ nm, $P_{10} = 10$ mW, $P_{20} = 5$ mW and $L = 1000$ m, Fig. 10(b) again displays satellite power as a function of fiber length, and the interfered-constructive dots marked with blue color meet the condition of $z = (2l + 1)\pi/(a - b)$. Moreover, interfered-destructive points marked with green and red dots satisfy the condition of $z = 4l\pi/(a - b)$ and $z = 2(2l + 1)\pi/(a - b)$, respectively. Also, the numerical simulation is in line with the analytical solution in this case. In fact, there have been some common points between the property of satellite wave evolvement and the coherent-superimposed principal. First, Eq. (38) for satellite power is similar with the expression for the intensity of interference pattern [17,18]. Second, for the coherent-superimposed principal, constructive and destructive points depend critically on the optical-path difference (identified with the phase difference) of two injected waves when they reach some point in space. Similarly, when the satellite wave travels to a specific location in an optical fiber, difference of different sets of phase-mismatch profiles in MFWM processes determines whether the fringe is bright or dark, corresponding to the constructive or destructive point.

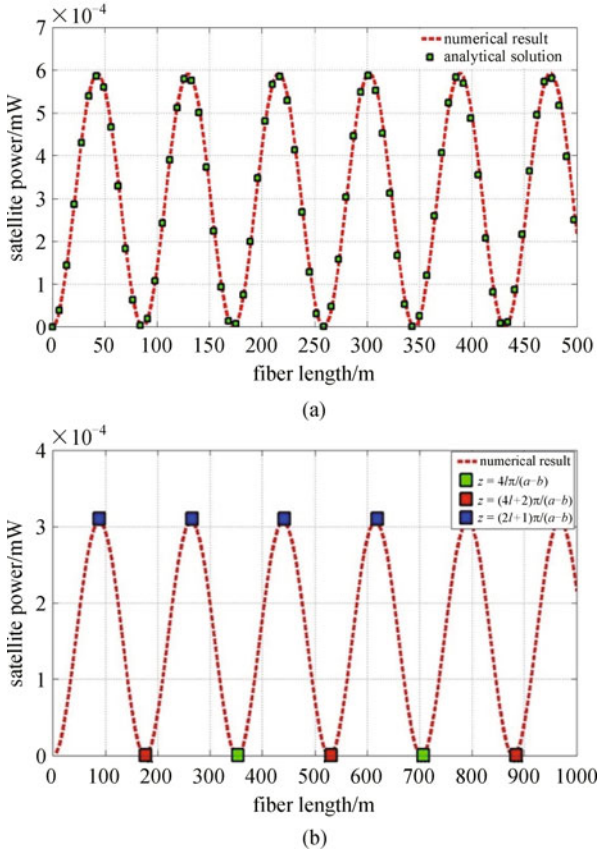

Fig. 10 Simulations for satellite power as a function of fiber length. (a) The red dash line represents the numerical result while the green dots denote the analytical solution. The related parameters are $\lambda_1 = 1555$ nm, $\lambda_2 = 1545$ nm, $P_{10} = 20$ mW, $P_{20} = 10$ mW and $L = 500$ m; (b) The green and red dots correspond to interfered-destructive points satisfying the condition of $z = 4l\pi/(a - b)$ and $z = (4l + 2)\pi/(a - b)$ respectively, the blue dots correspond to interfered-constructive points satisfying the condition of $z = (2l + 1)\pi/(a - b)$. The related parameters are $\lambda_1 = 1555$ nm, $\lambda_2 = 1548$ nm, $P_{10} = 10$ mW, $P_{20} = 5$ mW and $L = 1000$ m

Figure 11 illustrates satellite power as a function of fiber length with different injected wavelengths to check how the injected wavelength influences the periodic characteristic, as described by $T = [|T_a|, |T_b|, |T_{a-b}|]$. When $\lambda_1 = 1555$ nm and $\lambda_2 = 1548$ nm, one can easily obtain $T_a = -176.9358$ m, $T_b = -88.4493$ m, $T_{a-b} = 176.8615$ m, and thus $T \approx 176.8615$ m, which matches well with the numerical simulation shown in Fig. 11(a). Moreover, Figs. 11(b), 11(c) and 11(d) further demonstrate that, the period changes dramatically when setting different injected wavelengths, which implies that the values of T_a, T_b and T_{a-b} significantly rely on the injected wavelength. This characteristic is very useful in the applicative regime, especially for the optical switch and the logic gate [21], that we can obtain the satellite power to a largest extent by prudently selecting the injected wavelength provided the fiber length is fixed.

5 Conclusions

The nonlinear interaction between four optical fields involves a single non-degenerate (Mode C) and two degenerate FWM (Modes A and B) processes in the third-order nonlinear mixings, and we emphasize Mode C by simplifying the coupled-wave equations into the eigen-equations, as well as analyzing the phase-space trajectory. The existence of unstable eigensolutions has important consequences for evolution of each wave and the power exchange. Our solutions permit one to predict high-efficiency wavelength conversion for initially mismatched waves, and approximate 100% injected-wave power could be presumably coupled into the sideband wave, as long as we properly set the boundary condition. Furthermore,

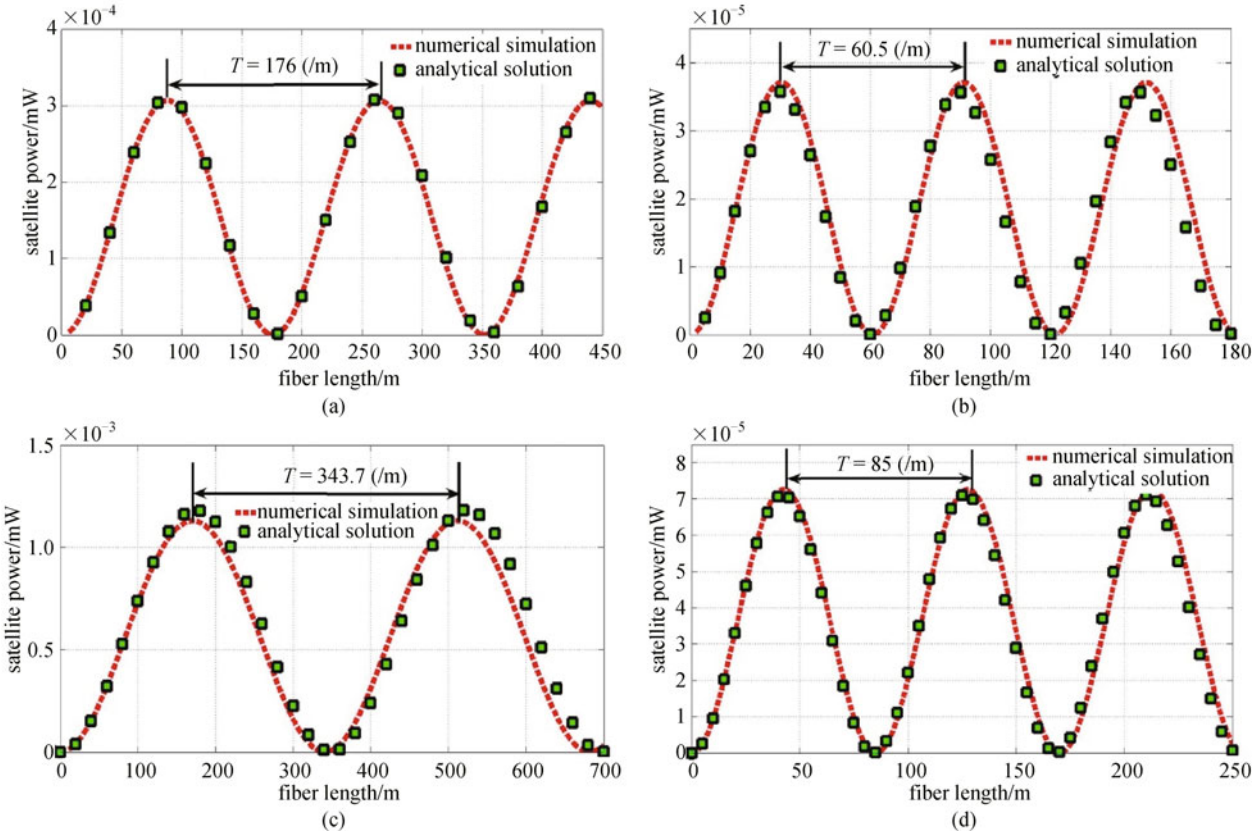

Fig. 11 Satellite power as function of fiber length with different injected wavelengths: (a) $\lambda_1 = 1555$ nm, $\lambda_2 = 1548$ nm; (b) $\lambda_1 = 1560$ nm, $\lambda_2 = 1548$ nm; (c) $\lambda_1 = 1550$ nm, $\lambda_2 = 1545$ nm; (d) $\lambda_1 = 1550$ nm, $\lambda_2 = 1540$ nm. The other parameters are $P_{10} = 10$ mW, $P_{20} = 5$ mW

under the condition of equalized and approximately-equalized injected powers, we have investigated phase-space orbits intensively by analyzing the type of singular point to judge the amount of power exchange. Finally, we demonstrate the characteristic of satellite wave by yielding the solution for its power analytically from the coupled-wave equations under certain approximations, and compare the evolvement of satellite wave with the interference pattern in Young's double-slit experiment. The above investigations can be found potential applications in 2R regeneration [7,8], optical switching [5], multi-channel all optical wavelength conversion [2], and UWB generation and transmission [22].

Acknowledgements This paper was supported by the National Basic Research Program of China (No. 2011CB301704), the National Natural Science Foundation of China (Grant Nos. 60901006 and 61106046), and the Youth Science Funds (No. 51109215).

References

1. Islam M N, Boyraz Ö. Fiber parametric amplifiers for wavelength band conversion. IEEE Journal of Quantum Electronics, 2002, 8(3): 527–537
2. Geraghty D F, Lee R B, Verdiell M, Ziari M, Mathur A, Vahala K J. Wavelength conversion for WDM communication systems using four-wave mixing in semiconductor optical amplifiers. IEEE Journal of Quantum Electronics, 1997, 3(5): 1146–1155
3. Hansryd J, Andrekson P A, Westlund M, Li J, Hedekvist P O. Fiber-based optical parametric amplifiers and their applications. IEEE Journal of Quantum Electronics, 2002, 8(3): 506–520
4. Hedekvist P O, Karlsson M, Andrekson P A. Fiber four-wave mixing demultiplexing with inherent parametric amplification. Journal of Lightwave Technology, 1997, 15(11): 2051–2058
5. Zhao Y. All-optical power-controlled switching in four-wave mixing. Optics Letters, 1989, 14(19): 1085–1087
6. Nie Z Q, Zheng H B, Zhang Y, Zhao Y, Zuo C, Li C, Chang H, Xiao M. Experimental demonstration of optical switching and routing via four-wave mixing spatial shift. Optics Express, 2010, 18(2): 899–905
7. Ciaramella E, Trillo S. All-optical signal reshaping via four-wave mixing in optical fibers. IEEE Photonics Technology Letters, 2000, 12(7): 849–851
8. Ciaramella E, Curti F, Trillo S. All-optical signal reshaping by means of four-wave mixing in optical fibers. IEEE Photonics Technology Letters, 2001, 13(2): 142–144
9. Liu X M, Zhou X Q, Lu C. Multiple four-wave mixing self-stability

in optical fibers. Physical Review A, 2005, 72(1): 013811
10. Liu X M, Zhou X Q, Lu C. Four-wave mixing assisted stability enhancement: theory, experiment, and application. Optics Letters, 2005, 30(17): 2257–2259
11. Cappellini G, Trillo S. Third-order three-wave mixing in single-mode fibers: exact solutions and spatial instability effects. Journal of the Optical Society of America. B, Optical Physics, 1991, 8(4): 824–838
12. Trillo S, Wabnitz S, Kennedy T A. Nonlinear dynamics of dual-frequency-pumped multiwave mixing in optical fibers. Physical Review A, 1994, 50(2): 1732–1747
13. Cappellini G, Trillo S. Energy conversion in degenerate four-photon mixing in birefringent fibers. Optics Letters, 1991, 16(12): 895–897
14. Trillo S, Wabnitz S. Dynamics of the nonlinear modulational instability in optical fibers. Optics Letters, 1991, 16(13): 986–988
15. Zhao L, Sun J Q. Investigation of tunable trap filter utilizing intense signal four wave mixing model in highly non-linear fiber. Optics Communications, 2009, 282(14): 2975–2982
16. Marhic M E, Wong K K Y, Ho M C, Kazovsky L G. 92% pump depletion in a continuous-wave one-pump fiber optical parametric amplifier. Optics Letters, 2001, 26(9): 620–622
17. Gachet D, Brustlein S, Rigneault H. Revisiting the Young's double slit experiment for background-free nonlinear Raman spectroscopy and microscopy. Physical Review Letters, 2010, 104(21): 213905
18. Intonti F, Riboli F, Caselli N, Abbarchi M, Vignolini S, Wiersma D S, Vinattieri A, Gerace D, Balet L, Li L H, Francardi M, Gerardino A, Fiore A, Gurioli M. Young's type interference for probing the mode symmetry in photonic structures. Physical Review Letters, 2011, 106(14): 143901
19. Liu X M. Theory and experiments for multiple four-wave-mixing processes with multifrequency pumps in optical fibers. Physical Review A, 2008, 77: 043818
20. Hart D L, Judy A F, Roy R, Beletic J. Dynamical evolution of multiple four-wave-mixing processes in an optical fiber. Physical Review E: Statistical Physics, Plasmas, Fluids, and Related Interdisciplinary Topics, 1998, 57(4): 4757–4774
21. Wu B B, Fu S N, Wu J, Shum P, Ngo N Q, Xu K, Hong X, Lin J. Simultaneous implementation of all-optical OR and AND logic gates for NRZ/RZ/CSRZ ON-OFF-keying signals. Optics Communications, 2010, 283(3): 349–354
22. Zhao L, Sun J Q, Huang D. Photonic generation of ultrawideband signals by exploiting gain saturation of dark pump pulse with double undershoots in a highly nonlinear fiber. Optics Communications, 2011, 284(6): 1669–1676